

## TRENDS IN ASYMMETRIC DRIFT ACROSS THE BLUE CLOUD

KYLE B. WESTFALL<sup>1</sup>, MATTHEW A. BERSHADY<sup>2</sup>, KEVIN BUNDY<sup>1</sup>, ET AL.

*Draft: 22 Jan 2018*

### ABSTRACT

Asymmetric drift (AD) is the lag of the mean rotation velocity of the stellar disk behind the circular speed defined by the total gravitational potential. Although it is often considered a nuisance correction one must apply in circular-speed calculations, the direct connection between AD and the stellar phase-space distribution function makes it an interesting dynamical property of galaxies in and of itself. The SDSS-IV/MaNGA survey provides more than an order of magnitude increase in any galaxy sample size useful for AD measurements. In this pilot study, we measure AD — or more precisely the differential tangential lag between the stellar component and H $\alpha$ -emitting gas — in a set of galaxies with H $\alpha$  and stellar velocity fields that are well-fit by simple disk models. We describe our fitting approach and the selection of our subsample in detail. Our final sample of  $\sim$ XXX galaxies shows a clear correlation between absolute  $i$ -band magnitude and AD measured at effectively all radii. **[[The rest needs to be updated.]]** Removing the primary dependence on the rotation speed, we find that the stellar disk rotation is 90% of the H $\alpha$  rotation speed, in the mean. Our sample size allows us to infer a weak, yet statistically significant, trend with galaxy  $N - r$  color such that, in the mean, redder galaxies have moderately larger AD relative to their rotation speeds. Within the context of an albeit strong set of assumptions, including a direct proportionality between AD and stellar velocity dispersion as seen in the Milky Way, we argue that our results suggest little variation in the mean disk mass-to-light ratio as a function of absolute magnitude and only modest variations with galaxy color **[[last sentence TBD; is Figure 3 consistent with SPS variations?]]**.

*Keywords:* galaxies: kinematics and dynamics — galaxies: spiral — galaxies: structure

### 1. MOTIVATION

For ensembles of stars in a galaxy disk, Binney & Tremaine (2008, Section 4.4.3) provide an intuitive description of asymmetric drift (AD). The combined effect of the radially decreasing surface-density and velocity-dispersion profiles, typical of axisymmetric systems like the Milky Way, leads to an asymmetric velocity distribution function with a mean value less than the circular speed defined by the gravitational potential. The standard mathematical representation of this is derived by taking the  $v_R$  moment of the collisionless Boltzmann equation to find the Jeans equation (Jeans 1919) that directly relates the circular speed ( $v_c$ ), the mean stellar tangential speed ( $\overline{v_\theta}$ ), and the stellar velocity ellipsoid (SVE) as a function of radius in the plane of symmetry:

$$v_c^2 - \overline{v_\theta}^2 = \sigma_R^2 \left[ \frac{\sigma_\theta^2}{\sigma_R^2} - \frac{R}{\rho \sigma_R^2} \frac{\partial(\rho \sigma_R^2)}{\partial R} - 1 \right] - R \frac{\partial \overline{v_R v_z}}{\partial z}, \quad (1)$$

where  $R, \theta, z$  are the cylindrical coordinates,  $\rho$  is the volume density, and  $\sigma$  is the velocity dispersion. Along with the standard assumptions of dynamical equilibrium and negligible radial and vertical flows inherent to its derivation, equation 1 is often simplified by assuming the right-most term is negligible (cf. Amendt & Cuddeford 1991); i.e., there is negligible covariance between the radial and vertical motions as a function of perpendicular distance to the plane of symmetry.

Asymmetric drift has been measured in numerous systems, perhaps most notably in the Galaxy. For example, Dehnen & Binney (1998) have shown that populations of stars show a direct correlation between their velocity dispersion and the degree to which their mean rotation speed lags behind that of the Local Standard of Rest (LSR), much in line with the expectation provided by equation 1 (see also **[[more recent RAVE and RAVE+Gaia references]]**).

Asymmetric drift measurements in extragalactic systems are common in the literature **[[examples]]**; however, it is most often cast as a nuisance phenomenon that one must correct for when constructing circular-speed curves **[[refs]]**. The ubiquity and phenomenology of AD as a salient observable has not yet been studied for a statistically significant population of galaxies. Our aim is therefore to provide a first look at the correlation between AD measurements and basic broad-band photometric properties for a large sample of galaxies.

In addition to a basic characterization of the phenomenon, our interest in AD stems from its fundamental dynamical connection to the full phase-space distribution function of a galaxy's stars, as empirically demonstrated in the Milky Way. Indeed, Westfall et al. (2011) used AD to constrain the axial ratios of the SVE given direct measurements of the line-of-sight (LOS) stellar velocity dispersion,  $\sigma$ . Alternatively, if one can statistically constrain the shape of the SVE (e.g. Gerssen & Shapiro Griffin 2012), measurements of AD could then be used as a proxy for stellar  $\sigma$  via equation 1. Such an AD- $\sigma$  relation becomes attractive in the low-surface-brightness and low-velocity-dispersion regimes where direct measurements of  $\sigma$  are difficult and/or expensive. Adopting this paradigm

Electronic address: westfall@ucolick.org

<sup>1</sup> University of California Observatories, University of California Santa Cruz, 1156 High St., Santa Cruz, CA 95064, USA

<sup>2</sup> Department of Astronomy, University of Wisconsin–Madison, 475 N. Charter St., Madison, WI 53706, USA

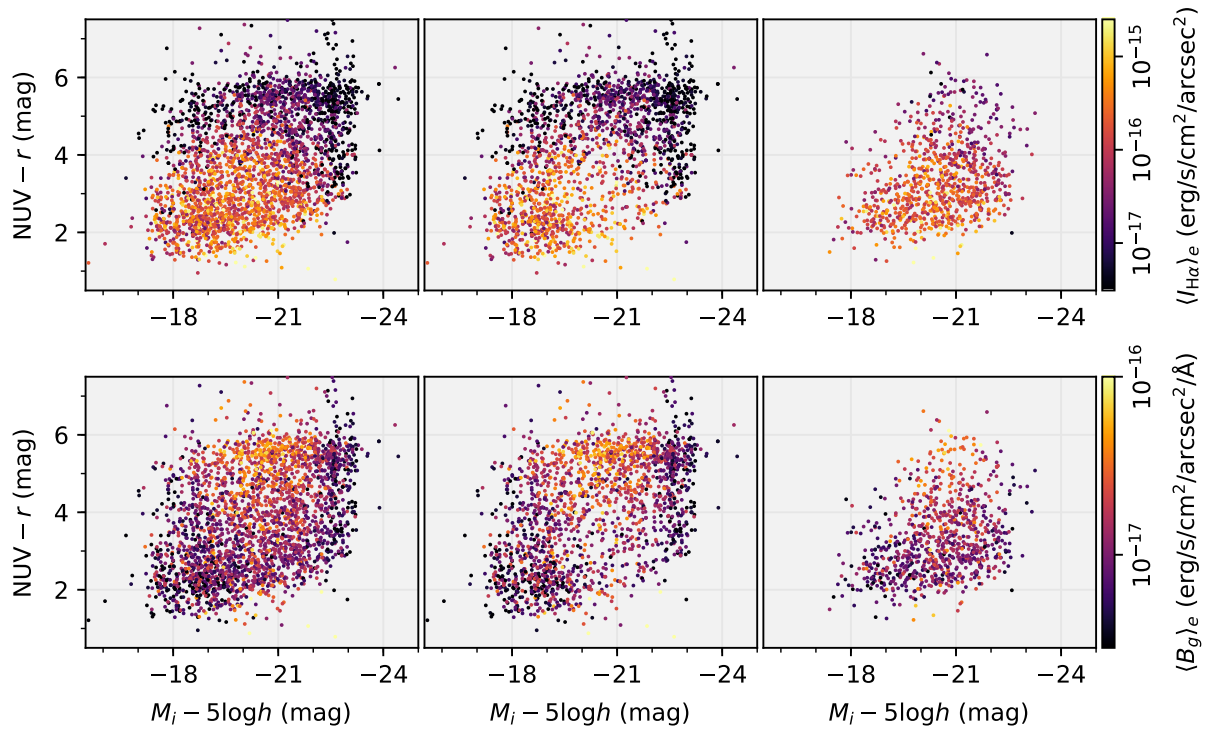


**Figure 1.** NUV  $- r$  color and absolute  $i$ -band magnitude ( $M_i$ ) from the NASA-Sloan Atlas (NSA) for all galaxies observed during the first two years of the MaNGA Survey (left), the subsample of galaxies *not* selected to be kinematically regular (middle; see text), and the AD sample used throughout the remainder of our analysis. The color of the data points in the top row represent the mean H $\alpha$  surface brightness within the elliptical-Petrosian half-light radius according to the colorbar to the right; the bottom row replaces the color by the mean  $g$ -band surface brightness density over the same elliptical aperture.

outright, we define  $\sigma_a^2 \equiv v_c^2 - \overline{v_\theta^2}$ , following from equation 1, for use throughout this paper.

For disk galaxies, there is a decades-long industry of using cold-gas tracers to construct circular-speed curves of galaxies [refs]. These data have provided the first concrete arguments for the presence of massive dark-matter halos [ref] based on mass-model reconstruction [refs] and have formed the basis for the most robust Tully-Fisher relations compiled for the local Universe [refs]. However, it is important to acknowledge that one cannot directly measure  $v_c$ , effectively making  $\sigma_a$  unobservable. That is, every tracer has some non-zero dynamical pressure such that it will lag behind the theoretically defined circular speed. There are very clear examples of early-type galaxies that show differential AD in their molecular (e.g., CO), atomic (e.g., H I), and/or ionized (H $\alpha$ ) tracers relative to a robust mass model of  $v_c$  (Davis et al. 2013) due to the different turbulent/thermal pressures intrinsic to these tracers. However, these signatures are much less apparent in disk galaxies. For example, Martinsson et al. (2013a) show that H $\alpha$  and H I rotation curves are consistent for the DiskMass Survey within the limits of their constraints on beam-smearing. This suggests that any correction for the lag behind the circular speed of either the H $\alpha$ - or H I-emitting gas should be small. Indeed, theoretical calculations Dalcanton & Stilp (2010) suggest that gas-pressure corrections to H I rotation curves should be largely negligible for galaxies with circular speeds larger than roughly  $75 \text{ km s}^{-1}$ . Nevertheless, we emphasize here that our measurements of

$\sigma_a$  may be better termed as a *differential tangential lag* because they are calculated as the quadrature difference between the *observed* H $\alpha$  and stellar rotation curves in our galaxy sample (Section 2). These measurements are perfectly valid in their own right; however, their interpretation in the context of the theoretical definition of AD must be done with care, as we discuss in Section 5.

**[[Outline should be updated]]** We present the data used for our analysis in the following section. Section 4 presents the strong correlation seen in our galaxy sample between the absolute  $i$ -band magnitude and AD signal measured at half of an effective radius ( $0.5 R_{\text{eff}}$ ). We also illustrate the weak color dependence in this relation. Finally, we summarize and discuss these results in Section 5. **[[flesh out]]**

## 2. DATA

### 2.1. Galaxy Sample

We use integral-field spectroscopy from the SDSS-IV/MaNGA (Mapping Nearby Galaxies from APO) Survey to construct stellar and ionized-gas velocity fields for 2715 unique galaxies, 39 of which have multiple observations. These data were obtained during the first two years of normal survey operations, and the reduced datacubes are included in DR14 (Abolfathi et al. 2017). **[[additional references to technical papers]]**.

The MaNGA galaxy selection is discussed in detail by Wake et al. (2017); the galaxies in DR14 represent a random sampling of full MaNGA parent sample. The parent sample is selected using simple cuts in

absolute  $i$ -band magnitude,  $M_i$ , and redshift,  $z$ , from the NASA-Sloan Atlas (NSA; [www.nsatlas.org](http://www.nsatlas.org)) to produce two main galaxy samples, Primary and Secondary, with roughly twice as many galaxies observed from the former. The main distinguishing characteristic of the two samples is MaNGA provides uniform coverage to  $\sim 1.5R_e$  and  $\sim 2.5R_e$  for the Primary and Secondary sample, respectively. The Primary sample is supplemented by a “Color-enhanced” sample that improves coverage of the galaxy population in low-density regions of color-magnitude space; the combination of Primary and Color-enhanced samples are referred to as the Primary+ sample. Although we will comment on any difference in our analysis results between the Primary+ and Secondary samples, we largely treat these two samples identically in our analysis.

The  $(N - r, M_i)$  color-magnitude diagram (CMD) for MaNGA galaxies in DR14 (using NSA photometry) is shown in the left-most panels of Figure 1. Data in the top and bottom row are colored according to, respectively, the average  $H\alpha$  surface brightness and  $g$ -band-weighted mean flux density within  $1 R_e$ . We discuss Figure 1 in the context of our selection of galaxies appropriate for our AD analysis [\[below\]](#).

## 2.2. MaNGA Spectroscopy

The MaNGA fiber-feed system Drory et al. (2015) for the 2.5-meter Sloan telescope at Apache Point Observatory (APO) is coupled to the SDSS-III/BOSS spectrographs (Smee et al. 2013), a pair of dual-channel spectrographs that provide  $R_\lambda = \lambda/\Delta\lambda \approx 2000$  across the full spectral range of  $3600\text{\AA} \lesssim \lambda \lesssim 10300\text{\AA}$ . Each MaNGA pointing provides simultaneous observations of 17 galaxies using fiber bundles ranging from 19 to 127 fibers. The dither pattern of the MaNGA observational strategy (Law et al. 2015) provides a remarkably uniform depth for each observation with fields-of-view ranging from  $12''$  to  $32''$  for the smallest and largest bundles, respectively. The uniform depth yields a tight correlation between flux density per spaxel and signal-to-noise (S/N); see Law et al. (2015); ? and Yan et al. (2016b,a) for additional details about the survey execution and performance.

In particular, ? describes the methods used by the MaNGA Data Reduction Pipeline (DRP) is an to produce wavelength-, flux- (Yan et al. 2016b), and astrometrically calibrated spectra from the raw CCD data. The reduction procedures are similar to those used by the SDSS-III/BOSS pipeline, but with significant adjustments as required by the MaNGA observations.

Here, we use the rectified datacubes that have been logarithmically binned in wavelength (i.e., the LOGCUBE files). The MaNGA data cubes are constructed by regridding the flux of all spectra for a given plate-IFU combination in each wavelength channel to an on-sky pixel (spaxel) sampling of  $0''.5 \times 0''.5$ . The interpolating PSF used in this process is a two-dimensional Gaussian with a standard deviation of  $0''.6$  and a truncation radius of  $1''.7$ . This interpolation process leads to significant covariance between the spaxels in a given wavelength channel (?). This spatial covariance does not affect the primary result of our paper, so we defer a more detailed consideration of the covariance for future work.

## 2.3. Stellar and Ionized-Gas Kinematics

The kinematic measurements are determined by a preliminary version (2.0.2) of the MaNGA Data Analysis Pipeline (DAP; Westfall et al., *in prep*). The pipeline provides simple single-Gaussian fits to the  $H\alpha$  emission feature that we use for the ionized-gas kinematics, and the stellar kinematics are determined using pPXF (Cappellari & Emsellem 2004; Cappellari 2017). The templates used by pPXF are a hierarchically clustered distillation of the MILES stellar template library (Falcón-Barroso et al. 2011). We find the velocity measurements to be statistically well behaved to a  $g$ -band signal-to-noise ratio of  $S/N \sim 1$ .<sup>3</sup> Therefore, we perform our analysis using the spaxel-by-spaxel determination of the stellar and ionized-gas kinematics.<sup>4</sup>

## 3. VELOCITY-FIELD MODELING

### 3.1. Formalism

We fit the  $H\alpha$  and stellar velocity fields using an approach similar to Andersen & Bershadsky (2013) (? , see also Westfall et al. 2011) The velocity field is modeled as an infinitely thin disk in fully circular rotation that follows a parameterized form  $V_{\text{rot}}(R)$ ; here we use a simple hyperbolic tangent function:

$$V_{\text{rot}}(R) = V_\infty \tanh(R/h_{\text{rot}}), \quad (2)$$

where  $V_\infty$  is the asymptotically flat rotation speed and  $h_{\text{rot}}$  is a characteristic scale for the rise of the rotation curve, and the model line-of-sight (LOS) velocity is

$$V_{\text{los}}(x, y) = V_{\text{rot}}(R[x, y]) \cos(\theta[x, y]) \sin i + V_{\text{sys}} \quad (3)$$

where  $i$  is the disk inclination (a “face-on” disk has  $i = 0$ ), and  $V_{\text{sys}}$  is the systemic velocity of the galaxy. The disk-plane polar coordinates  $(R, \theta)$  in Equation 3 are functions of the on-sky position:

$$x_d = (x + x_0) \sin \phi_0 + (y + y_0) \cos \phi_0 \quad (4)$$

$$y_d \cos i = -(x + x_0) \cos \phi_0 + (y + y_0) \sin \phi_0 \quad (5)$$

$$R^2 = x_d^2 + y_d^2 \quad (6)$$

$$\tan \theta = -y_d/x_d, \quad (7)$$

where  $(x, y)$  is the on-sky position ( $+x$  is to the east) relative to the center of the object as defined by the targeting catalog,  $(x_0, y_0)$  is the location of this pointing center of the IFU relative to the dynamical center,  $\phi_0$  is the position angle defined from north through east of the receding side of the major axis, and  $(x_d, y_d)$  are the disk-plane Cartesian coordinates. Note that  $\theta = 0^\circ$  along the major axis on the receding side of the galaxy.

**[REST IS OLD TEXT]**

[We emphasize that this parametrization is used in the determination of the kinematic geometry from the rotation curve, but not as measurements of the rotation speed itself (see Section XX).]

Provided  $j = 0 \dots N_{\text{spaxels}}$  LOS velocity measurements,  $V_{\text{los},j}$ , and their errors,  $\epsilon_{v,j}$ , we determine the best-fitting model velocity field using a Levenberg-Marquardt mini-

<sup>3</sup> This and other assessments of the fidelity of the stellar kinematics provided by the DAP will be discussed in detail by Westfall et al., *in prep*.

<sup>4</sup> However, note that only the stellar kinematic determined for data Voronoi binned to  $S/N \sim 10$  will be provided as part of DR15.

mization algorithm with the following figure-of-merit:

$$\chi^2 = \sum_j \frac{(V_{\text{los},j} - V_{\text{mod}}[x_j, y_j])^2}{\epsilon_{v,j}^2 + \epsilon_{\text{mod}}^2}, \quad (8)$$

where  $\epsilon_{\text{mod}}$  is an intrinsic scatter of the measured LOS velocities about the simplistic model. To simplify further discussion, we denote the  $j$  components of the sum on the right-hand of the equation as  $\chi_j^2$ . [[Go back and include the “beam-smearing” term?]]

In an effort to minimize the well-known covariance between the inclination and rotation speed (refs), our velocity-field parameterization actually fits the *projected* rotation curve (i.e.,  $V_{\text{rot}}(R) \sin i$ ) instead of the disk-plane rotation speed itself. The fitted parameters for a single velocity field are then  $x_c, y_c, i, \phi_0, V_{\text{sys}}, V_{\infty} \sin i$ , and  $h_{\text{rot}}$ .

### 3.1.1. Implementation details

The description in Section ?? [apart from leaving out the beam-smearing term] is identical to the approach of Andersen & Bershadsky (2013). The alterations specific to our implementation are as follows (cf. Westfall et al. 2011):

1. *Simultaneous VF fitting*: We have extended the code from Andersen & Bershadsky (2013) to allow for simultaneous fits to multiple dynamical tracers, while allowing the rotation curves of the two components to be different. Although we do fit the H $\alpha$  and stellar data fit independently, this is primarily used in the selection cuts imposed in Section 3.2.5. When fitted simultaneously, there are three additional free parameters compared to those listed above: the two additional rotation curve parameters and systemic velocity of the second dynamical tracer. That is, even when fitting the two velocity fields simultaneously, we allow for the systemic velocities of the two tracers to be different. This is primarily to allow for, e.g., systematic errors in the velocity registration of the template libraries used to determine the stellar kinematics. Ideally, one would like to force the systemic velocities of the two tracers to be the same, and we discuss the effects on our results by allowing them to be different in Section 3.2.
2. *Intrinsic scatter*: The intrinsic scatter term,  $\epsilon_{\text{mod}}$ , serves a number of purposes. Its effect is to alter the error-weighted distribution of the fit residuals such that it closely follows a Gaussian distribution with unity standard deviation; that is, it forces the reduced  $\chi^2$ ,  $\chi_{\nu}^2$ , of the fit to be very close to unity. Indeed, Andersen & Bershadsky (2013) chose  $\epsilon_{\text{mod}}$  such that  $\chi_{\nu}^2 \sim 1$  to within 1%. Our approach is to instead iteratively adjust  $\epsilon_{\text{mod}}$  until the growth curve of  $\chi_j^2$  is marginally different from the growth curve of a Gaussian function with unity standard deviation. This approach is primarily chosen given its advantage in dealing with our third alteration. [[Affect on formal parameter errors from the covariance matrix.]]
3. *Measurement Rejection*: The fits to the velocity fields generally provide  $\chi_{\nu}^2 > 1$  when  $\epsilon_{\text{mod}} = 0$ ,

meaning that there is a general systematic discrepancy of model with respect to the  $V_{\text{los}}$  measurements that is not accounted for by the random errors,  $\epsilon_{v,j}$ . Although most of the discrepancies can be accounted for by a small ( $\epsilon_{\text{mod}} \sim XX$ ) scatter about the simplistic model, systematic error in the kinematic measurements, particularly at low SNR, can lead to a number of  $V_{\text{los},j}$  with  $\chi_j^2 \gg 1$ . We iteratively reject these data from the fit at the same time as we determine the intrinsic scatter term,  $\epsilon_{\text{mod}}$ . After fitting the data with a given  $\epsilon_{\text{mod}}$  (starting with 0), we iteratively reject points with  $\chi_j^2 > 1$ , starting with the largest value, and adjust  $\epsilon_{\text{mod}}$  until the root-mean-square difference between the growth curve of  $\chi_j^2$  and a Gaussian with unity standard deviation is minimized. This whole process of fitting the velocity field, determining  $\epsilon_{\text{mod}}$ , and rejecting aberrant data is done many times to make sure that the points that are rejected and the value of  $\epsilon_{\text{mod}}$  is not strongly biased by the initial fit to the velocity field.

### 3.1.2. Initialization

The MaNGA data cubes (cf. Law et al. *in prep*) provide an accurate registration of the spectrophotometry with on-sky imaging data to provide a detailed astrometric calibration in the form of a world-coordinate system (WCS) in the fits headers. The coordinates of the targeted galaxy<sup>5</sup> are, in general, exactly the coordinates provided by the NASA-Sloan Atlas; however, some coordinates have been adjusted to better match the galaxy center [[check this with David W.]] (cf., Wake et al. *in prep*). The  $(x, y)$  coordinate system in Eqn. 3 is then established by setting the  $(0, 0)$  coordinate at the galaxy center. Thus, when freely fit, we should expect to find  $x_0 = y_0 = 0$  arcsec.

The NASA-Sloan Atlas also provides ellipticity and position angle measurements for isophotal contours of each galaxy, which we use as the initial guesses for the kinematic inclination and position angle, respectively. For an oblate spheroid with intrinsic axial ratio  $q_0$  and an observed ellipticity of  $\varepsilon = 1 - b/a$ , its inclination to the LOS is given by (ref)

$$\cos^2 i_{\text{phot}} = \frac{(1 - \varepsilon)^2 - q_0^2}{1 - q_0^2}. \quad (9)$$

For our measurements of  $i_{\text{phot}}$ , we assume  $q_0 = 1/8$  (Bershadsky; but, cf., Weijmanns).

Given that our definition of  $\phi_0$  is tied to the vector along the major axis toward the receding side of the velocity field, the kinematic position angle has a valid range of  $2\pi$ . However, photometric position angles only have a valid range of  $\pi$ . Our initial guess of  $\phi_0$  is either the same as the photometric value or flipped by  $180^\circ$  based on an initial deprojection of the rotation speed along the photometric position angle.

Finally, we use the redshift provided by the NASA-Sloan Atlas as the initial estimate of the systemic velocity,  $V_{\text{sys}} = cz_{\text{NSA}}$ .

<sup>5</sup> This is generally the center of the data cube field-of-view; however, some observations were purposely offset for testing purposes.

### 3.1.3. Fitting iterations

We expect AD to be present in all galaxies, and so we attempt to fit all 1392 galaxies in the current MaNGA sample. For such a large galaxy sample, it is difficult to attempt human interaction at a detailed level with each fit. Therefore, all of the fits have been performed in an automated way. To help in the quality assessments of the fits (Sections 3.2 and 3.2.5), we fit the velocity fields of each tracer ( $H\alpha$ -emitting gas and stars) both individually and in a single, simultaneous fit. Additionally, we perform the individual and simultaneous fits under permutations of fixing and freeing the inclination and center.

The determination of  $V_{\text{sys}}$  and  $\phi_0$  are generally robust and well-constrained by the data, meaning there is no need to fix them to certain values. Conversely, the inclination and center can be poorly determined in certain regimes. For example, when the observed velocity field is that of a solid-body rotator, the isovelocity contours all become parallel to the minor axis ( $V_{\text{rot}} \propto R$  and, at a fixed perpendicular distance from the minor axis,  $\cos \theta \propto R^{-1}$ ). Thus, in the absence of any other information, one could place the center anywhere in the velocity field without affecting  $\chi^2$ . Similarly, measurements of inclination depend on the curvature seen in the isovelocity contours and there is no such curvature for a solid-body rotator. Finally, at low inclination, the curvature in the isovelocity contours can be imperceptible due to the stochastic deviations (random and systematic) about the fitted model. Therefore, by performing fits that both fix and free the center and inclination, we can test the consistency of the results and the significance of kinematically constrained parameters versus simply adopting the photometric one.

In addition, we impose boundaries on the allowed range for the geometric parameters. We force the systemic velocity to be within  $\pm 1000 \text{ km s}^{-1}$  of the input guess, we force  $0.1 \leq i \leq 85$  and  $0 \leq \phi_0 < 360$ , and we define a bounding box for the fitted center to be  $\sim 20\%$  of the full field-of-view. The limits for the IFUs with 19, 37, 61, 91, and 127 fibers are limited to  $\pm 1''$ ,  $\pm 2''$ ,  $\pm 2''$ ,  $\pm 3''$ , and  $\pm 3''$ , respectively.

In summary, we perform 12 velocity-field fits for each galaxy: (1) four fits are permutations of fixing and freeing the center and inclination and (2) each of these four fits is done when only fitting the  $H\alpha$  data, only fitting the stellar data, and fitting both tracers simultaneously.

## 3.2. Kinematic Geometry Results

For our AD measurements, we require robustly measured kinematic geometries that can be applied to both the  $H\alpha$ -emitting and stellar components. This requirement drives our assessments of the kinematic geometries and the selection of galaxies to propagate through our AD analysis in the remaining sections of the paper. For example, it is physically plausible to find a significant offsets between the position angles of gas and stars (e.g., Chen et al.; Belfiore et al.); however, this is typically the signature of an accretion event and not conducive to an AD measurement. Given the fits that we have performed, we can check both the consistency of the  $H\alpha$  and stellar geometries, as well as their consistency with the morphological geometry.

We first limit our assessments to those galaxies with

successfully converged velocity-field fits for all 12 fit iterations, which cuts our sample from 1392 to 1322 galaxies. [[Should maybe have a sentence about why these failed?]] All subsequent cuts include this base-level selection.

### 3.2.1. Systemic velocity

When fit separately, the best-fitting systemic velocities for both the  $H\alpha$  and stellar data are in good agreement with each other and with the redshifts in the NASA-Sloan Atlas,  $cz_{\text{NSA}}$ . The mean difference with respect to  $cz_{\text{NSA}}$  over the full 1322 galaxies is less than  $10 \text{ km s}^{-1}$  and the standard deviation is approximately the velocity width of a spectral channel ( $\sim 70 \text{ km s}^{-1}$ ), regardless of the fitting constraints or tracer.

The result is approximately the same when considering the difference between the  $H\alpha$ -only and stellar-only fit parameters. Indeed, we should expect that the systemic velocity should be the same for the  $H\alpha$  and stellar components; however, we have allowed them to be different, even when fitting the two velocity fields simultaneously. Fig. 2(a) shows the distribution of  $V_{\text{sys},H\alpha} - V_{\text{sys},*}$  when both are fit simultaneously. After applying a 3-sigma clipping algorithm, we find a mean difference of  $2.3 \pm 6.8 \text{ km s}^{-1}$ . It is difficult to understand how this systematic offset could arise either physically or due to a wavelength-calibration error. We therefore assume that this mean offset is due to a systematic error in the velocity registration of the MIUSCAT template spectra across our fitted wavelength range. Further work is required to exactly address this problem; however, it has a minimal effect on our analysis [[need to test this]].

To avoid the strong outliers, particular toward the negative end of Fig. 2(a), we select only those galaxies with  $-12.5 \text{ km s}^{-1} \leq V_{\text{sys},H\alpha} - V_{\text{sys},*} \leq 17.5 \text{ km s}^{-1}$  for further analysis; 850 of 1322 galaxies (64%) meet this criterion.

### 3.2.2. Pointing relative to the dynamical center

In Section 3.1.3, we noted that the pointing relative to the dynamical center ( $x_0, y_0$ ) has a bounding box placed on it that is IFU-dependent. When selecting results for our AD analysis, we care more about the fitted center relative to the bounding box than we do about the absolute center in arcseconds. Therefore, in Fig. 2(b) we show the ratio of the fitted center relative to the size of the bounding box — e.g.,  $-1 \leq \tilde{x}_0 \leq 1$  — for both on-sky coordinates. Recall (Section ??) the definition of our  $(x, y)$  coordinate system is such that a result of  $(x_0, y_0) = (0, 0)$  means that the morphological and dynamical centers are co-located.

The results in Fig. 2(b) are specifically for the case where we have fit both tracers simultaneously. We find that the simultaneous fit to both tracers reduces the scatter about the morphological center compared to the result for the fits to an individual tracer: the standard deviations are 0.52, 0.44, and 0.39 for the  $H\alpha$ , stellar, and combined fits, respectively. Under the expectation that the morphological and dynamical centers should be the same for dynamically settled galaxies, we force both  $\tilde{x}_0$  and  $\tilde{y}_0$  to be within  $\pm 0.5$ , of which 926/1322 (70%) of the galaxies satisfy. Before applying this selection, the standard deviation of  $(x_0, y_0)$  is approximately 0.9 for each coordinate, which is reduced by a factor of 3 for the selected sample of 926 galaxies.



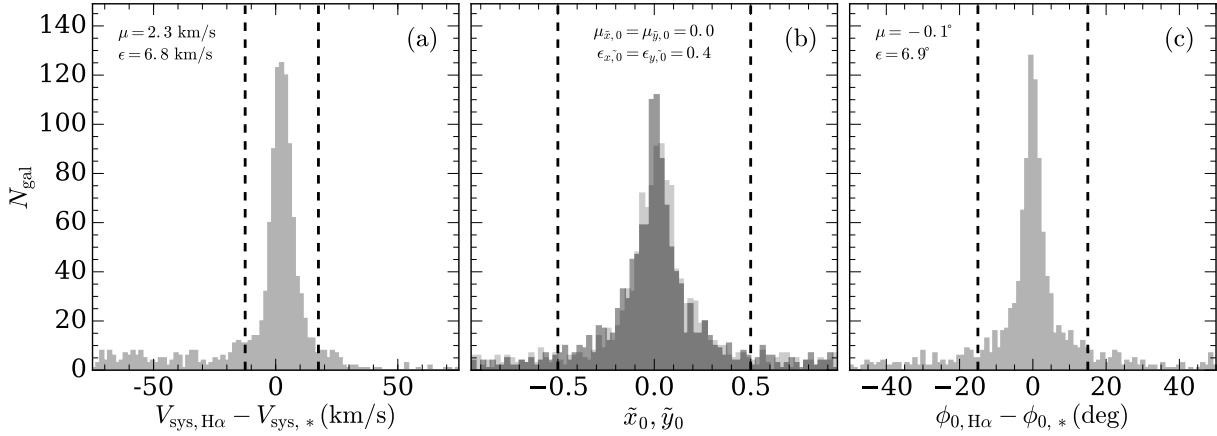


**Figure 2.** Distribution of (a) the difference between the H $\alpha$  and stellar systemic velocities; (b) the center relative to the imposed fit boundary; and (c) the difference between the H $\alpha$  and stellar kinematic position angles. For the center panel, the distributions of  $\hat{x}_0$  and  $\hat{y}_0$  are shown as (transparent) light and dark histograms, respectively. The 3-sigma clipped mean ( $\mu$ ) and standard deviation ( $\epsilon$ ) for each distribution is provided in associated panel. The dashed lines illustrate the cuts that we adopt for each parameter in our AD analysis (see text).

### 3.2.3. Position angle

The kinematic position angle is periodic with an imposed range in the fit of  $0 \leq \phi_0 \leq 360$ . In calculating the difference between any two position angles, we account for this range and periodicity such that the difference in position angle should be centered at  $0^\circ$ , as is the case when comparing  $\phi_{0,H\alpha}$  and  $\phi_{0,*}$  in Fig. 2(c). Although physical differences in the fitted position angles are interesting for other reasons (earlier refs; Chen et al.; Belfiore et al.), our measurements of AD benefit from selecting galaxies where the position angles are very similar.

In contrast with the other two panels in Fig. 2, panel (c) compares the results when each dynamical tracer is fit independently. We find a standard deviation in the difference of  $7^\circ$  after iteratively clipping at 3-sigma. We have chosen to select only those galaxies with H $\alpha$  and stellar derived  $\phi_0$  that differ by less than  $15^\circ$ , which selects 832 of the 1322 (63%) galaxies. Although our selection criterion for  $\phi_0$  is based on the H $\alpha$ -only and stellar-only fits, we note that the calculation of AD *assumes the position angle obtained from the simultaneous fit to both tracers*. The 3-sigma clipped standard deviation of the difference between  $\phi_{0,H\alpha}$  or  $\phi_{0,*}$  and the result when both are fit simultaneously is  $\sim 1^\circ$ .

### 3.2.4. Inclination

In Fig. 3, we compare the photometric inclinations (see eqn. 9) with the kinematic inclinations determined from the H $\alpha$ -only ( $i_{H\alpha}$ ), stellar-only ( $i_*$ ), and simultaneous ( $i_{*+H\alpha}$ ) velocity-field fits, illustrating the progression of our inclination selection criteria.

The top-left panel of Fig. 3 shows that the fitted inclinations for a significant number of galaxies are biased by our imposed fit boundaries. Therefore, we first only consider galaxies with kinematic inclinations that are between  $15^\circ < i_{\text{kin}} < 80^\circ$ . Even after imposing this limit, however, we find  $i_{H\alpha} - i_* \approx -1^\circ \pm 16^\circ$ . The difference between  $i_{*+H\alpha}$  and either  $i_{H\alpha}$  or  $i_*$  has an understandably smaller scatter of  $\pm 11^\circ$ . If we simultaneously impose the constraints outlined above for  $V_{\text{sys}}$ ,  $(x_0, y_0)$ , and  $\phi_0$ , we are left with 622 of 1322 galaxies that have  $i_{H\alpha} - i_* \approx -2^\circ \pm 12^\circ$ , as shown in the top-right panel of

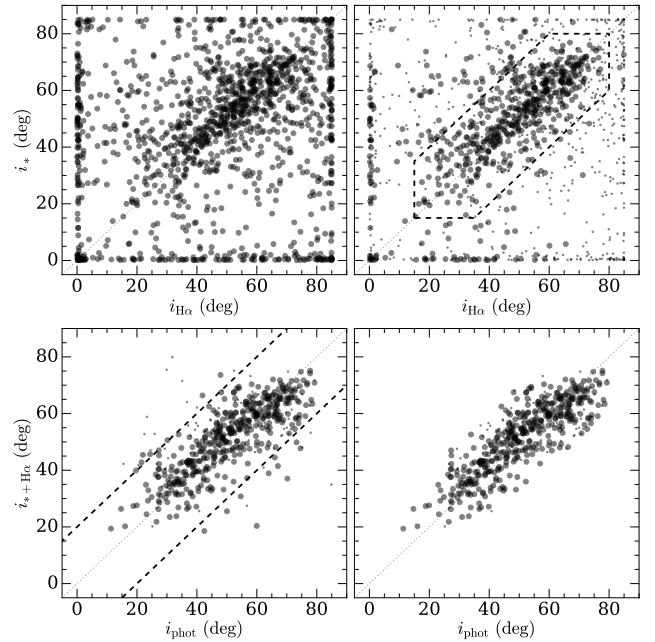


**Figure 3.** Comparison of the three kinematic inclinations — as resulting from the H $\alpha$ -only ( $i_{H\alpha}$ ), stellar-only ( $i_*$ ) and simultaneous ( $i_{*+H\alpha}$ ) fits — with the photometric inclination,  $i_{\text{phot}}$  (see eqn. 9). From top-left to bottom-right, the panels illustrate the progression of our inclination-based selection criteria. The gray dotted line shows the 1:1 correspondence in all panels. (*Top row*): Comparison of  $i_{*+H\alpha}$  (abscissa) and  $i_*$  (ordinate) for all 1322 galaxies with successful velocity-field fits. The top-left panel shows the distribution before any selection criteria are applied, whereas the top-right panel converts the point type for galaxies that are *not* selected by the constraints on  $V_{\text{sys}}$ ,  $(x_0, y_0)$ , and  $\phi_0$  to small points. In the top-right panel, the dashed polygon represents our primary inclination criterion. (*Bottom row*): Comparison of  $i_{\text{phot}}$  (abscissa) with  $i_{*+H\alpha}$  (ordinate); large dots and small points have the same meaning as in the top-right panel. The bottom-left panel shows all galaxies that pass our primary inclination criterion, whereas the bottom-right panel shows only those galaxies that satisfy both criteria (see text). The dashed lines in the bottom-left panel illustrate our secondary inclination criterion.

Fig. 3. Based on this distribution, our primary inclination selection is  $15^\circ < i_{\text{kin}} < 80^\circ$  and  $|i_{\text{H}\alpha} - i_*| < 20^\circ$ . When applied to fits both with and without the center fixed, the criterion is satisfied by 524 of the 1322 galaxies.

Our secondary criterion checks for consistency of  $i_{*+\text{H}\alpha}$  and  $i_{\text{phot}}$ , which is shown in the bottom-left panel of Fig. 3. After imposing only the primary inclination criterion, we find  $i_{*+\text{H}\alpha} - i_{\text{phot}} = 0^\circ \pm 10^\circ$ ; the scatter decreases to  $\pm 9^\circ$  if we also apply the  $V_{\text{sys}}$ ,  $(x_0, y_0)$ , and  $\phi_0$  criteria. Our secondary inclination criterion imposes  $|i_{*+\text{H}\alpha} - i_{\text{phot}}| < 20^\circ$ , such that the full sample is shown as filled dots in the bottom-right panel of Fig. 3. The combination of the two inclination criteria yields our most stringent selection cut, limiting our sample from 1322 to 487 galaxies.

[[Note the systematic offset between the kinematic and photometric inclinations at  $i_{\text{phot}} \gtrsim 60^\circ$ . Known inadequacy of the infinitely thin model. Check the effect this has on the AD- $\sigma$  distribution.]]

### 3.2.5. Summary of selection cuts

In summary, our AD- $\sigma$  analysis is of galaxies that satisfy the following set of constraints on the results from the velocity field fitting:

1. When the two velocity fields are fitted simultaneously, the difference between the systemic velocities fit to the H $\alpha$  and stellar velocity fields must be within  $-12.5 \text{ km s}^{-1} \leq V_{\text{sys,H}\alpha} - V_{\text{sys},*} \leq 17.5 \text{ km s}^{-1}$  for *all* four of the fit permutations.
2. In the two simultaneous fits to the H $\alpha$  and stellar data with the dynamical center left free, the dynamical center must be within half of the imposed bounding box on the morphological center.
3. For *all* the relevant fit permutations, the difference between the H $\alpha$ -only and stellar-only fitted position angles must be less than  $15^\circ$ .
4. In *all* six fits when the inclination is freely fit, the best-fitting kinematic inclination must be in the range  $15^\circ < i_{\text{kin}} < 80^\circ$ . The difference between the H $\alpha$ -only and stellar-only kinematic inclinations must be less than  $20^\circ$  both with and without a fixed center. When both tracers are fit simultaneously, the kinematic inclination must also be within  $20^\circ$  of the photometric inclination (eqn. 9).

The simultaneous application of all these cuts yields a sample of 413 galaxies from the original set of 1322.

We model the geometric projection of the rotational plane of each galaxy using the approach presented by (Andersen & Bershady 2003, see also Westfall et al. 2011). In three independent fitting iterations, the model fits are optimized for the H $\alpha$  velocity field, the stellar velocity field, and simultaneously for both data sets; for the latter, the geometry is forced to be the same for the two dynamical tracers, but the parametrized rotation curves are independent. We use these velocity-field-fitting results to objectively isolate a set of “kinematically regular” galaxies. Briefly, galaxies in this sample must have: (i) successful velocity-field fits for all three approaches, (ii) differences in the measured H $\alpha$  and stellar systemic velocity of less than  $20 \text{ km s}^{-1}$ , (iii) dynamical centers

that are consistent to within a fiber diameter of the morphological center **[[check the details of this]]**, (iv) H $\alpha$  and stellar velocity-field position angles that are consistent to within  $\pm 15^\circ$ , and (v) kinematic inclinations between  $15^\circ < i < 80^\circ$  that are both consistent between the H $\alpha$  and stellar data and with respect to the photometric ellipticity to within  $\pm 20^\circ$ . The constraint on the inclination is by far the most stringent. **[[give number of galaxies cut by each criterion?]]** Applying these constraints yields a sample of 798 observations (for 790 unique galaxies) out of the 2764 observations analyzed. Eleven galaxies with repeat observations satisfy the selection criteria; however, only five of these show all observations are consistently selected. The remaining six show one or more of the observations did not pass our constraints **[[we should understand why repeat observations are not consistent for the majority of cases. low S/N?]]**. **[[Do this or remove the sentence:]]** Finally, we also visually inspected the broad-band imaging of these 790 galaxies and eliminated merging and highly extincted (highly inclined) systems yielding a final sample of XXX galaxies. We hereafter refer to galaxies that satisfy our selection criteria as the “AD sample”.

**[[limitations of an infinitely thin disk fit?]]**

Figure 1 shows the color-magnitude distribution for all MaNGA galaxies, as well as the distributions of those galaxies included and excluded from our AD sample. As expected, galaxies with relatively high H $\alpha$  and  $r$ -band surface brightness are preferentially selected. This results in an exclusion of much of the red sequence, as well as the brightest and faintest galaxies in the blue cloud. Although the conclusions we reach based on our AD sample are astrophysically meaningful, it is important to appreciate that the galaxies in our AD sample are a biased representation of the overall galaxy population.

**[[Show histogram of kinematically regular sample against the volume-corrected distribution of the MaNGA parent sample in Mi and N-r, and discuss?]]**

Our velocity-fitting method provides a model rotation curve fit to both the H $\alpha$  and stellar data, each parametrized as a hyperbolic tangent function:  $v_{\text{rot}} = v_{\text{flat}} \tanh(R/h_v)$ . However, our primary result is based on the error-weighted mean of the deprojected rotation-curve measurements for each dynamical tracer. We only include measurements within  $\pm 30^\circ$  of the major axis and construct radial bins that are  $2''.5$  wide and centered at 0.25, 0.5, 0.75, 1.0, and  $1.25 R_{\text{eff}}$  —  $R_{\text{eff}}$  is the effective radius using the elliptical Petrosian analysis from the NASA-Sloan Atlas. **[[Check if the  $R_{\text{eff}}$  does or does not include the multiplicative offset to match these Petrosian and Sersic  $R_{\text{eff}}$  in the mean.]]** Specifically, we calculate the error-weighted mean and standard deviation of  $v_j = V_j / \cos \theta_j / \sin i$  and

$$\sigma_{a,j}^2 = (V_{\text{H}\alpha,j}^2 - V_{*,j}^2)(\cos \theta_j \sin i)^{-2}, \quad (10)$$

where  $V_j$  is the LOS measurement of each component in spaxel  $j$  located at the in-plane polar coordinates  $R_j$  and  $\theta_j$  and  $i$  is the disk inclination.

**[[An example demonstrating the details of our measurements is illustrated in Figure X.]]**

**Table 1**  
Linear Regressions for  $M_i$  **[[check m-b form]]**

Parameter	Dependent Variable		
	$\log(v_{H\alpha})$	$\log(\sigma_a^2)$	$\log(\sigma_a/v_{H\alpha})$
$y_0$	2.168 $\pm 0.003$	3.78 $\pm 0.01$	-0.269 $\pm 0.003$
$\phi$	170.70 $\pm 0.15$	160.1 $\pm 0.5$	-0.24 $\pm 0.17$
$\varepsilon$	0.069 $\pm 0.001$	0.209 $\pm 0.005$	0.068 $\pm 0.002$
$m$	-0.164 $\pm 0.003$	-0.362 $\pm 0.009$	-0.004 $\pm 0.003$
$b$	-1.20 $\pm 0.05$	-3.69 $\pm 0.19$	-0.36 $\pm 0.06$
$\varepsilon_y$	0.070 $\pm 0.001$	0.222 $\pm 0.005$	0.068 $\pm 0.002$

We calculate errors in  $v_{H\alpha}$  and  $\sigma_a$  as the quadrature sum of the error-weighted standard error (i.e., the error-weighted standard deviation divided by  $\sqrt{N}$ ) and the propagated error in the error-weighted mean. **[[Should we revisit this? Details of error calculation not all that important. We're dominated by intrinsic deviations in the regressions below.]]**

#### 4. RESULTS

Figure 4(a) shows the  $(M_i, N-r)$  color-magnitude diagram (see right column of Figure 1) with the points colored according to  $\sigma_a$  measured at  $R = 0.5R_{\text{eff}}$ . There is a clear trend where brighter galaxies have larger  $\sigma_a$ ; the remainder of the Figure examines this trend.

We plot  $M_i$  versus  $v_{H\alpha}$ ,  $\sigma_a^2$ , and  $\sigma_a/v_{H\alpha}$  in Figures 4(b), 4(c), and 4(d), respectively. The points are colored according to the label to the right of each color bar. Each panel provides the Spearman rank-correlation coefficient,  $r_s$ , of the plotted data with errors derived from  $10^3$  bootstrap simulations. We have also used a Markov Chain Monte Carlo to sample the Bayesian posterior distribution for a linear regression to the data in each panel, incorporating the errors in both axes (see, e.g. Hogg et al. 2010); the errors in the kinematic quantities always dominate over the absolute magnitude errors. The fitted model is a line in parametric form with an intrinsic Gaussian scatter perpendicular to the line. That is, the line is defined as  $\mathbf{l}(t) = \mathbf{l}_0 + t \hat{\mathbf{l}}$  for a generalized coordinate  $t$  along the line, an origin  $\mathbf{l}_0 = \{x_0, y_0\}$ , and the unit vector  $\hat{\mathbf{l}} = \{\cos \phi, \sin \phi\}$ . The fitted parameters are  $y_0$ ,  $\phi$ , and the dispersion of the intrinsic Gaussian scatter about the line,  $\varepsilon$ ;  $x_0$  is fixed at the median abscissa of the data being fitted ( $M_{i,0} = -20.6$ ). Uniform priors are used for  $y_0$  and  $\phi$  and a logarithmic prior **[[check this is true]]** is used for  $\varepsilon$  (MacKay 2003). Using the returned samples of the posterior, we also provide parameters for the slope-intercept form of the line —  $y = mx + b$  where  $m = \tan \phi$  and  $b = y_0 - x_0 \tan \phi$  — and the scatter projected along the ordinate,  $\varepsilon_y = \varepsilon / |\cos \phi|$ . Table 1 provides the median and standard deviation of the marginalized distribution of each parameter; these parameters have been used to construct the lines provided in Figure 4.

**[[Show the PDFs?]]**

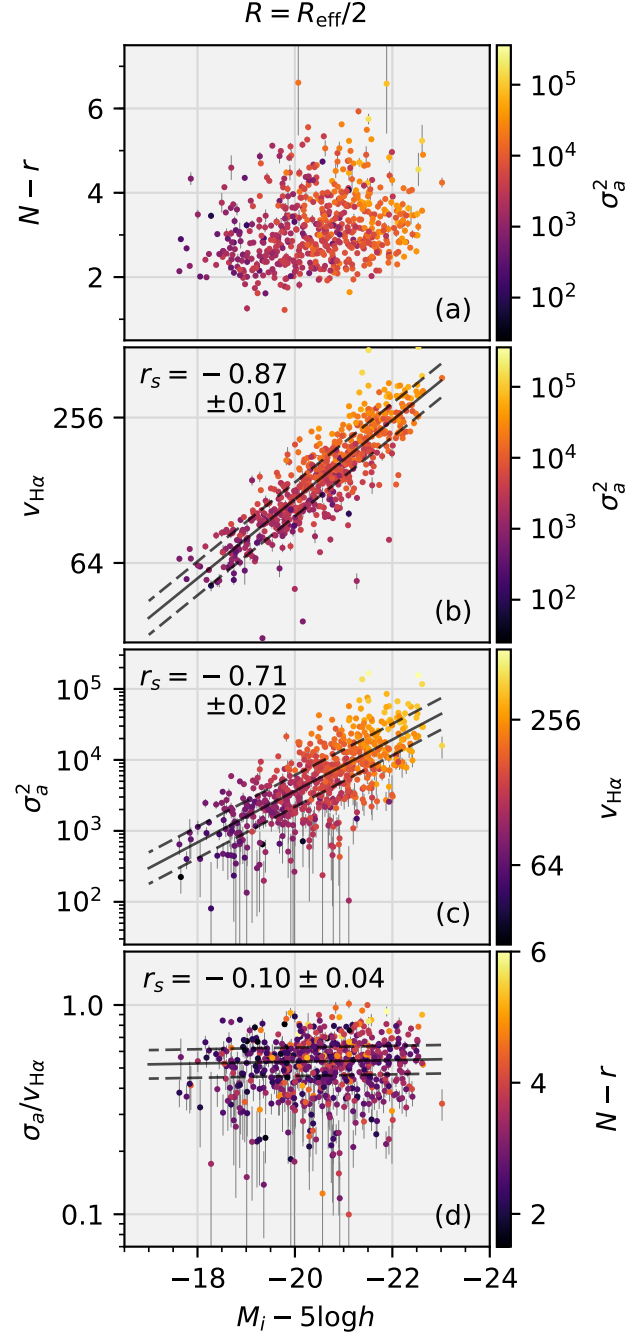


**Figure 4.** Global photometry and kinematic measurements at  $R = R_{\text{eff}}/2$  for the AD sample:  $M_i$  versus (a)  $N-r$  color with each point colored according to  $\sigma_a^2$ , (b)  $v_{H\alpha}$  with each point colored according to  $\sigma_a^2$ , (c)  $\sigma_a^2$  with each point colored according to  $v_{H\alpha}$ , and (d)  $\sigma_a/v_{H\alpha}$  with each point colored by the  $N-r$  color. Panels (b), (c), and (d) include the Spearman rank correlation coefficient,  $r_s$ , and the linear regressions (solid lines) constructed from the parameters provided in Table 1. The dashed lines are offset from linear regression by the modeled intrinsic scatter in the relation ( $\varepsilon_y$ ).



As expected, there is a strong correlation between  $v_{H\alpha}$  and  $M_i$ . However, it is important to note that Figure 4(b) does not present the Tully & Fisher (1977) relation for our AD sample; the Figure gives the rotation speed at  $R = 0.5R_{\text{eff}}$ , not a measure of the full-width of the dynamically broadened line profile. The slope of the relation in Figure 4(b) is steeper than a nominal Tully-Fisher relation because galaxies at low luminosity tend to have more slowly rising rotation curves **[[refs]]**, which can be confirmed by plotting  $h_{v,H\alpha}/R_{\text{eff}}$  as a function of  $M_i$ . **[[actually show this?]]**

Figure 4(c) gives the direct representation of the gradient in the point color seen in Figure 4(a). The data in this panel are highly correlated, both as determined by  $r_s$  and the fitted regression. The intrinsic scatter increases from 0.07 dex (17%) in  $(M_i, v_{H\alpha})$  to 0.21 dex (62%) in  $(M_i, \sigma_a^2)$ ; however, this is close to the  $\sim 0.1$  dex scatter if considering  $(M_i, \sigma_a)$  instead.

If  $\sigma_a$  or  $v_{H\alpha}$  was a fully orthogonal secondary parameter in the distribution of  $(M_i, v_{H\alpha})$  or  $(M_i, \sigma_a^2)$ , respectively, we should expect a gradient in the point color in Figures 4(b) and 4(c) *perpendicular* to the fitted regression. However, we see that the primary gradient in point color is parallel to the fitted regression. This is consistent with the result that there is little to no correlation between  $M_i$  and  $\sigma_a/v_{H\alpha}$ , as shown in Figure 4(d): Both  $r_s$  and  $\phi$  are small and only marginally significant with respect to their errors. From equation 10, this implies that the deprojected stellar rotation is roughly a constant fraction of the ionized-gas rotation speed, with  $v_* \sim 0.9v_{H\alpha}$  **[[give scatter]]**. Although the radius at which the AD was sampled is different, this ratio is consistent with a similar ratio measured for DiskMass-Survey galaxies (Martinsson et al. 2013b).

**[[Need to revisit this paragraph in the context of the bulge-to-disk fraction.]]** The points in Figure 4(d) are colored by the global  $N - r$  color. It is difficult to determine from this illustration if there is any correlation between  $\sigma_a/v_{H\alpha}$  and global galaxy color. One might expect such a correlation if, for example, galaxies with different global color have different light-weightings of the thin- vs. thick-disk **[[refs; not sure there are relevant ones; Comerón?]]**, which propagates to a difference in which component dominates the dynamical pressure in the disk midplane. Figure 5 assesses this directly by plotting the error-weighted mean trend in  $\sigma_a/v_{H\alpha}$  for quartiles of the  $N - r$  distribution of the AD sample. The error bars represent the error-weighted standard deviation of the data in each bin, whereas the error-weighted standard error is always *smaller than the plotted point*. This suggests a marginal, yet statistically significant, detection of a slightly larger  $\sigma_a/v_{H\alpha}$  in the reddest bin.

## 5. DISCUSSION

### 5.1. Technical Concerns

**[[Sample bias]]**  
**[[Beam-smearing]]**

### 5.2. Prospects

**[[If  $\sigma_a$  is a direct proxy for  $\sigma_R$  ...]]**

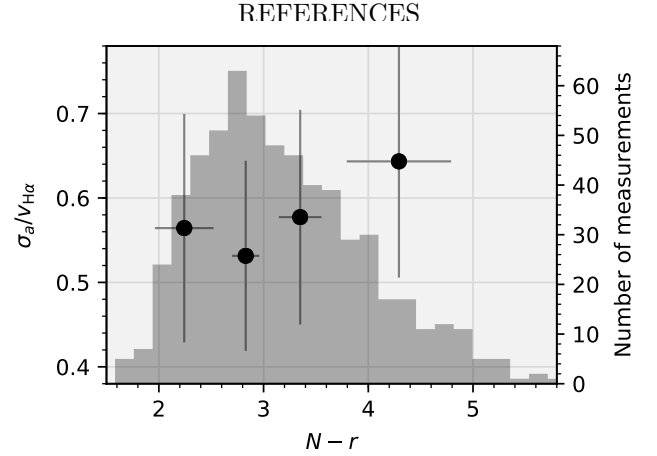


**Figure 5.** The error-weighted mean trend in  $\sigma_a/v_{H\alpha}$  binned in quartiles of the global  $N - r$  color (black points). The error bars represent the error-weighted standard deviation of the data within each bin; the error-weighted standard error is smaller than the size of each black point. The underlying gray histogram provides the number of measurements in bins of  $N - r$ ; each quartile contains  $\sim 152$  galaxies.

- Abolfathi, B., Aguado, D. S., Aguilar, G., et al. 2017, ArXiv e-prints, arXiv:1707.09322  
 Amendt, P., & Cuddeford, P. 1991, ApJ, 368, 79  
 Andersen, D. R., & Bershadsky, M. A. 2003, ApJ, 599, L79  
 —. 2013, ApJ, 768, 41  
 Binney, J., & Tremaine, S. 2008, Galactic Dynamics: Second Edition (Princeton University Press, Princeton, NJ USA)  
 Cappellari, M. 2017, MNRAS, 466, 798  
 Cappellari, M., & Emsellem, E. 2004, PASP, 116, 138  
 Dalcanton, J. J., & Stilp, A. M. 2010, ApJ, 721, 547  
 Davis, T. A., Alatalo, K., Bureau, M., et al. 2013, MNRAS, 429, 534  
 Dehnen, W., & Binney, J. J. 1998, MNRAS, 298, 387  
 Drory, N., MacDonald, N., Bershadsky, M. A., et al. 2015, AJ, 149, 77  
 Falcón-Barroso, J., Sánchez-Blázquez, P., Vazdekis, A., et al. 2011, A&A, 532, A95  
 Gerssen, J., & Shapiro Griffin, K. 2012, MNRAS, 423, 2726  
 Hogg, D. W., Bovy, J., & Lang, D. 2010, arXiv:1008.4686, arXiv:1008.4686  
 Jeans, J. H. 1919, Phil. Trans. R. Soc. London A, 218, 157  
 Law, D. R., Yan, R., Bershadsky, M. A., et al. 2015, AJ, 150, 19  
 MacKay, D. J. C. 2003, Information Theory, Inference, and Learning Algorithms (Cambridge University Press), available from <http://www.inference.phy.cam.ac.uk/mackay/itila/>  
 Martinsson, T. P. K., Verheijen, M. A. W., Westfall, K. B., et al. 2013a, A&A, 557, A131  
 —. 2013b, A&A, 557, A130  
 Smee, S. A., Gunn, J. E., Uomoto, A., et al. 2013, AJ, 146, 32  
 Tully, R. B., & Fisher, J. R. 1977, A&A, 54, 661  
 Wake, D. A., Bundy, K., Diamond-Stanic, A. M., et al. 2017, AJ, 154, 86  
 Westfall, K. B., Bershadsky, M. A., Verheijen, M. A. W., et al. 2011, ApJ, 742, 18  
 Yan, R., Bundy, K., Law, D. R., et al. 2016a, AJ, 152, 197  
 Yan, R., Tremonti, C., Bershadsky, M. A., et al. 2016b, AJ, 151, 8